SARS-CoV-2 spike P681R mutation enhances and accelerates viral fusion

Akatsuki Saito[1,2,3,16], Hesham Nasser[4,5,16], Keiya Uriu[6,16], Yusuke Kosugi[6,16], Takashi Irie[7,16], Kotaro Shirakawa[8], Kenji Sadamasu[9], Izumi Kimura[6], Jumpei Ito[6], Jiaqi Wu[10,11], Seiya Ozono[12], Kenzo Tokunaga[12], Erika P Butlertanaka[1], Yuri L Tanaka[1], Ryo Shimizu[4,13], Kenta Shimizu[14], Takasuke Fukuhara[14], Ryoko Kawabata[7], Takemasa Sakaguchi[7], Isao Yoshida[9], Hiroyuki Asakura[9], Mami Nagashima[9], Kazuhisa Yoshimura[9], Yasuhiro Kazuma[8], Ryosuke Nomura[8], Yoshihito Horisawa[8], Akifumi Takaori-Kondo[8], The Genotype to Phenotype Japan (G2P-Japan) Consortium, So Nakagawa[10,11]*, Terumasa Ikeda[4]*, Kei Sato[6,11,15,17]*.

[1] Department of Veterinary Science, Faculty of Agriculture, University of Miyazaki, Miyazaki 8892192, Japan
[2] Center for Animal Disease Control, University of Miyazaki, Miyazaki 8892192, Japan
[3] Graduate School of Medicine and Veterinary Medicine, University of Miyazaki, Miyazaki 8892192, Japan
[4] Division of Molecular Virology and Genetics, Joint Research Center for Human Retrovirus infection, Kumamoto University, Kumamoto 8600811, Japan
[5] Department of Clinical Pathology, Faculty of Medicine, Suez Canal University, Ismailia 41511, Egypt
[6] Division of Systems Virology, Department of Infectious Disease Control, International Research Center for Infectious Diseases, The Institute of Medical Science, The University of Tokyo, Tokyo 1088639, Japan
[7] Institute of Biomedical and Health Sciences, Hiroshima University, Hiroshima 7348551, Japan
[8] Department of Hematology and Oncology, Graduate School of Medicine, Kyoto University, Kyoto 6068507, Japan
[9] Tokyo Metropolitan Institute of Public Health, Tokyo 1690073, Japan
[10] Department of Molecular Life Science, Tokai University School of Medicine, Kanagawa 2591193, Japan
[11] CREST, Japan Science and Technology Agency, Saitama 3220012, Japan
[12] Department of Pathology, National Institute of Infectious Diseases, Tokyo 1628640, Japan
[13] Graduate School of Medical Sciences, Kumamoto University, Kumamoto 8600811, Japan
[14] Department of Microbiology and Immunology, Graduate School of Medicine, Hokkaido University, Hokkaido 0608638, Japan
[15] Twitter: @SystemsVirology
[16] These authors contributed equally

[17] Lead Contact
*Correspondences:
so@tokai.ac.jp (S.N.)
ikedat@kumamoto-u.ac.jp (T.Ikeda)
KeiSato@g.ecc.u-tokyo.ac.jp (K.Sato)

Conflict of interest: The authors declare that no competing interests exist.
Short title: A SARS-CoV-2 spike mutation promotes viral fusion (49/50 characters)
Keywords: SARS-CoV-2; COVID-19; spike protein; B.1.617; P681R; fusion

Highlights (85 characters including spaces)

- P681R mutation is highly conserved in the B.1.617 lineages
- P681R mutation accelerates and enhances SARS-CoV-2 S-mediated fusion
- Promotion of viral fusion by P681R mutation is augmented by TMPRSS2

Summary (150/150 words)

During the current SARS-CoV-2 pandemic, a variety of mutations have been accumulated in the viral genome, and at least five variants of concerns (VOCs) have been considered as the hazardous SARS-CoV-2 variants to the human society. The newly emerging VOC, the B.1.617.2 lineage (delta variant), closely associates with a huge COVID-19 surge in India in Spring 2021. However, its virological property remains unclear. Here, we show that the B.1.617 variants are highly fusogenic and form prominent syncytia. Bioinformatic analyses reveal that the P681R mutation in the spike protein is highly conserved in this lineage. Although the P681R mutation decreases viral infectivity, this mutation confers the neutralizing antibody resistance. Notably, we demonstrate that the P681R mutation facilitates the furin-mediated spike cleavage and enhances and accelerates cell-cell fusion. Our data suggest that the P681R mutation is a hallmark characterizing the virological phenotype of this newest VOC, which may associate with viral pathogenicity.

Introduction

In December 2019, an unusual infectious disease, now called coronavirus disease 2019 (COVID-19), emerged in Wuhan, Hubei province, China (Wu et al., 2020; Zhou et al., 2020). Severe acute respiratory syndrome coronavirus 2 (SARS-CoV-2), the causative agent of COVID-19, has rapidly spread all over the world, and as of June 2021, SARS-CoV-2 is an ongoing pandemic: more than 170 million cases of infections have been reported worldwide, and more than 3.5 million people died of COVID-19 (WHO, 2021a).

During the current pandemic, SARS-CoV-2 has acquired a variety of mutations [reviewed in (Plante et al., 2021)]. First, in the spring of 2020, a SARS-CoV-2 derivative harboring the D614G mutation in its spike (S) protein has emerged and quickly become predominant (Korber et al., 2020). Because the D614G mutation increases viral infectivity, fitness, and inter-individual transmissibility (Hou et al., 2020; Ozono et al., 2021; Plante et al., 2020; Volz et al., 2021; Yurkovetskiy et al., 2020; Zhou et al., 2021), the D614G-bearing variant has quickly swept out the original strain. Since the fall of 2020, some SARS-CoV-2 variants bearing multiple mutations have emerged and rapidly spread worldwide. As of June 2021, there have been at least five variants of concern (VOC): B.1.1.7 (alpha variant), B.1.351 (beta variant), P.1 (gamma variant), B.1.427/429 (epsilon variant; note that this variant has been downgraded to a variant of interest in May 2021) and B.1.617.2 (delta variant), and these lineages respectively emerged in the UK, South Africa, Brazil, the USA and India (CDC, 2021; WHO, 2021b).

As a common characteristic of VOCs, these variants tend to be relatively resistant to the neutralizing antibodies (NAbs) that were elicited in convalescent and vaccinated individuals [reviewed in (Corti et al., 2021; Harvey et al., 2021)]. In fact, recent investigations have revealed that B.1.1.7 (Chen et al., 2021; Collier et al., 2021; Wang et al., 2021b), B.1.351 (Chen et al., 2021; Garcia-Beltran et al., 2021; Hoffmann et al., 2021; Liu et al., 2021b; Planas et al., 2021; Wang et al., 2021b), P.1 (Garcia-Beltran et al., 2021; Hoffmann et al., 2021; Wang et al., 2021a) and B.1.427/429 (Deng et al., 2021) are differentially resistant to the NAbs derived from COVID-19 convalescents and vaccinees. Because the receptor binding domain (RBD) of SARS-CoV-2 S protein is immunodominant, approximately 90% of the NAbs present in anti-SARS-CoV-2 sera targets this domain (Piccoli et al., 2020). On the other hand, some SARS-CoV-2 variants including VOCs have acquired mutation in the RBD, such as the E484K mutation (Garcia-Beltran et al., 2021; Hoffmann et al., 2021), to evade antiviral immunity.

At the end of 2020, the B.1.617 lineage has emerged in India, and this variant is thought to be a main driver of a massive COVID-19 surge in India, which

has peaked 400,000 infection cases per day (Singh et al., 2021). The B.1.617 lineage includes three sublineages, B.1.617.1, B.1.617.2 and B.1.617.3, and a sublineage, B.1.617.2, is the latest VOC (CDC, 2021; WHO, 2021b). Importantly, early evidence from the Public Health England has suggested that the B.1.617.2 may have an increased risk of hospitalization compared to the B.1.1.7 cases (PHE, 2021).

Compared to the other VOCs, there are at least two common features in the S protein of the B.1.617 lineage. One is the L452R mutation, which is shared with the B.1.427/429 lineage. Because recent studies including ours have shown that the L452R mutation increases viral infectivity and fusogenicity (Deng et al., 2021; Motozono et al., 2021), the L452R mutation in the B.1.617 variant can contribute to the accelerated spread of this variant in the human population. The other is the substitution at the position 484 of S protein; the B.1.617.1 and B.1.617.3 variants possess the E484Q mutation, while the two VOCs, B.1.351 and P.1, possess E484K (CDC, 2021; WHO, 2021b).Intriguingly, both the E484K (Baum et al., 2020; Chen et al., 2021; Liu et al., 2021c; Wang et al., 2021b; Weisblum et al., 2020) and E484Q mutations (Ferreira et al., 2021) can contribute to the resistance to NAbs. In fact, recent studies have shown that the B.1.617.1 variant is resistant to the vaccine-induced NAbs (Edara et al., 2021; Liu et al., 2021a). In contrast to these two sublineages, the B.1.617.2 lineage possesses a unique mutation, T478K. A study has recently shown that the B.1.617.2 variant is also relatively resistant to the NAbs elicited by vaccination (Wall et al., 2021).

Interestingly, the P681R mutation in the S protein of B.1.617 lineage is a unique and newly identified mutation in the VOCs so far. Because the P681R mutation is located in the proximity of the furin cleavage site (FCS; residues RRAR positioned between 682-5) of the SARS-CoV-2 S protein (Shang et al., 2020), it is possible that this substitution affects viral replication dynamics and potentially determine the virological characteristics of the B.1.617 variants. In fact, recent investigations have revealed that the deletion of FCS modulates viral replication kinetics in *in vitro* cell cultures and *in vivo* animal models (Johnson et al., 2021; Peacock et al., 2021). However, it remains unclear which mutation(s) are responsible for the virological feature of this newly emerging VOC. In this study, we show that the P681R mutation enhances the cleavage of SARS-CoV-2 S protein. We further demonstrate that the P681R mutation enhances and accelerates viral fusion and promotes cell-cell infection.

Results

Phylogenetic and epidemic dynamics of the B.1.617 lineage

We set out to investigate the phylogenetic relationship of the three subvariants belonging to the B.1.617 lineage. We downloaded 1,761,037 SARS-CoV-2 genomes and information data from the Global Initiative on Sharing All Influenza Data (GISAID) database (https://www.gisaid.org; as of May 31, 2021). As expected, each of three sublineages, B.1.617.1, B.1.617.2 and B.1.617.3, formed a monophyletic cluster, respectively (**Figure 1A**). We then analyzed the epidemic of each of three B.1.617 sublineages. The B.1.617 variant, particularly B.1.617.1, was first detected in India on December 1, 2020 (GISAID ID: EPI_ISL_1372093) (**Figures 1B-1D**). Note that a SARS-CoV-2 variant (GISAID ID: EPI_ISL_2220643) isolated in Texas, the USA, on August 10, 2020, was also recorded to belong to the B.1.617.1. However, the S protein of this viral sequence (GISAID ID: EPI_ISL_2220643) possesses neither L452R nor P681R mutations, both of which are the features of the B.1.617 lineage. Therefore, the EPI_ISL_2220643 sequence isolated in the USA may not be the ancestor of the current B.1.617.1 lineage, and the EPI_ISL_1372093 sequence obtained in India would be the oldest B.1.617 lineage.

The B.1.617.2 (GISAID ID: EPI_ISL_2131509) and B.1.617.3 (GISAID IDs: EPI_ISL_1703672, EPI_ISL_1703659, EPI_ISL_1704392) were detected in India on December 10, 2020 and February 13, 2021, respectively (**Figures 1E and 1F**). The B.1.617.1 sublineage has peaked during February to April, 2021, in India, and then decreased (**Figure 1D**). Although the B.1.617.3 variant has sporadically detected in India (**Figure 1F**), the B.1.617.2 lineage has become dominant in India since March 2021 and spread all over the world (**Figure 1E**). At the end of May 2021, 100%, 70% and 43.3% of the deposited sequences in GISAID per day from India (May 7), the UK (May 21) and the whole world (May 19) have been occupied by the B.1.617.2 sublineage (**Figure 1E and Table S1**).

We next investigated the proportion of amino acid replacements in the S protein of each B.1.617 sublineage comparing with the reference strain (Wuhan-Hu-1; GenBank accession no. NC_045512.2). As shown in **Figure 1G**, the L452R and P681R mutations were highly conserved in the B.1.617 lineage, and notably, the P681R mutation (16,650/16,759 sequences, 99.3%) was the most representative mutation in this lineage. These data suggest that that the P681R mutation is a hallmark of the B.1.617 lineage.

Prominent syncytia formation by the B.1.617 variants

To investigate the virological characteristics of the B.1.617 variants, we conducted virological experiments using two viral isolates of B.1.617.1 (GISAID ID:

EPI_ISL_2378733) and B.1.617.2 (GISAID ID: EPI_ISL_2378732) as well as a D614G-bearing B.1.1 isolate (GISAID ID: EPI_ISL_479681) in Japan. In Vero cells, the growth of the B.1.617.1 and B.1.617.2 variants was significantly lower than that of the B.1.1 isolate (**Figure 2A**). Particularly, the levels of viral RNA of the B.1.617 variants at 48 hours postinfection (hpi) were more than 150-fold lower than that of the B.1.1 isolate (**Figure 2A**). On the other hand, although the growth kinetics of these three viruses was relatively comparable in VeroE6/TMPRSS2 cells (**Figure 2A**), microscopic observations showed that the VeroE6/TMPRSS2 cultures infected with these three viruses form syncytia. Notably, the two B.1.617 viruses formed larger syncytia compared to the B.1.1 virus (**Figure 2B**). By measuring the size of the floating syncytia in the infected VeroE6/TMPRSS2 culture, the syncytia formed by the B.1.617.1 and B.1.617.2 infection were significantly (2.3-fold and 2.7-fold) larger than that by the B.1.1 infection (**Figure 2B**). Immunofluorescence assay further showed that the two B.1.617 viruses form larger syncytia in VeroE6/TMPRSS2 cells compared to the B.1.1 isolate (**Figure 2C**). Altogether, these results suggest that the B.1.617 lineages are feasible for forming syncytia and relatively prefer cell-cell infection compared to the D614G-bearing B.1.1 virus.

P681R mutation as the determinant of the promotion and acceleration of S-mediated fusion

As shown in **Figure 1G**, the P681R mutation is a unique feature of the B.1.617 lineage. Because this mutation is located at the proximity of the FCS of SARS-CoV-2 S protein (Shang et al., 2020), we hypothesized that the P681R mutation is responsible for the preference of cell-cell fusion, which leads to larger syncytia formation, by the B.1.617 lineage. To address this possibility, we generated the P681R-bearing artificial virus by reverse genetics (**Figure 3A**) and preformed virological experiments. As shown in **Figure 3B**, the growth kinetics of the D614G/P681R mutant was significantly lower than that of the D614G mutant in Vero and VeroE6/TMPRSS2 cells. Although the viral RNA level at 72 hpi in VeroE6/TMPRSS2 cells was comparable between these two viruses (**Figure 3B**), the size of floating syncytia in the D614G/P681R mutant-infected culture was significantly larger than that in the D614G mutant-infected culture (**Figure 3C**). This observation well corresponds to that in the culture infected with the B.1.617 variants (**Figure 2B**). Moreover, although the viral RNA levels of these two viruses were comparable in HeLa-ACE2/TMPRSS2 cells (**Figure 3B**), prominent and large syncytia were observed only in the culture infected with the D614G/P681R mutant (**Figure 3C**).These results suggest that the feature of the B.1.617 viruses observed

in *in vitro* cell culture experiments, particularly forming larger syncytia (**Figure 2**), is well reproduced by the P681R mutation.

To directly investigate the effect of P681R mutation on the cleavage of SARS-CoV-2 S protein, we prepared the HIV-1-based pseudoviruses carrying the P681R mutation. Western blotting of the pseudoviruses prepared showed that the level of cleaved S2 subunit was significantly increased by the P681R mutation (**Figure 4A**), suggesting that the P681R mutation facilitates the furin-mediated cleavage of SARS-CoV-2 S protein. We then performed the single-round pseudovirus infection assay using the target HOS cells with or without TMPRSS2 expression. In the absence of TMPRSS2, the infectivity of the P681R/D614G-bearing pseudovirus was comparable to that of the D614G pseudovirus (**Figure 4B, left**). In the presence of TMPRSS2, the infectivity of the D614G pseudovirus increased at 5.0-6.3-fold compared to the TMPRSS2-null target cells (**Figure 4B, right**). Although the infectivity of the D614G/P681R pseudovirus also was increased by TMPRSS2 expression, it was significantly lower than the infectivity of the D614G pseudovirus (**Figure 4B, right**). These data suggest that the P681R mutation attenuates the infectivity of cell-free virus in the presence of TMPRSS2.

We next addressed the effect of P681R mutation on viral fusogenicity by cell-based fusion assay. In the effector cells (i.e., S-expressing cells), although the protein expression level of the D614G/P681R S was comparable to that of the D614G S, the level of the cleaved S2 subunit of the D614G/P681R mutant was significantly higher than that of the D614G S (**Figure 4C**). Consistent with the results in the pseudovirus assay (**Figure 4A**), these results suggest that P681R mutation facilitates the furin-mediated S cleavage. Flow cytometry showed that the surface expression level of the D614G/P681R S was significantly lower than the D614G S (**Figure 4D**). Nevertheless, the cell-based fusion assay using the target cells without TMPRSS2 demonstrated that the D614G/P681R S is 2.1-fold more fusogenic than the D614G S with a statistical significance ($P = 0.0002$ by Welch's t test) (**Figure 4E**). Moreover, a mathematical modeling analysis of the fusion assay data showed that the initial fusion velocity of the D614G/P681R S (0.83 ± 0.03 per hour) is significantly (2.8-fold) faster than that the D614G S (0.30 ± 0.03 per hour; $P = 4.0 \times 10^{-6}$ by Welch's t test) (**Figures 4F and 4G**). These data suggest that the P681R mutation enhances and accelerates the SARS-CoV-2 S-mediated fusion. Furthermore, when we use the target cells with TMPRSS2 expression, both the fusion efficacy (~1.2-fold) and initial fusion velocity (~2.0-fold) were increased in both the D614G and D614G/P681R S proteins (**Figures 4F and 4G**). These results suggest that TMPRSS2 facilitates the fusion mediated by SARS-CoV-2 S and human ACE2,

while the TMPRSS2-dependent acceleration and promotion of viral fusion is not specific for the P681R mutant.

Resistance to NAb-mediated antiviral immunity by the P681R mutation

The resistance to the NAb in the sera of COVID-19 convalescents and vaccinated individuals is a hallmark characteristic of the VOCs [reviewed in (Corti et al., 2021; Harvey et al., 2021)], and Liu et al. and Wall et al. recently showed that the B.1.617.1 (Liu et al., 2021a) and B.1.617.2 (Wall et al., 2021) variants are relatively resistant to the NAbs elicited by the BNT162b2 vaccination. To ask whether the P681R mutation contributes to this virological phenotype, we performed the neutralizing assay. As shown in **Figure 5A**, the D614G/P681R pseudovirus was partially (1.2-1.5-fold) resistant to the three monoclonal antibodies targeting the RBD of SARS-CoV-2 S protein. Additionally, the neutralizing experiments using the 19 sera of second BNT162b2 vaccination showed that the D614G/P681R pseudovirus is significantly resistant to the vaccine-induced NAbs compared to the D614G pseudovirus ($P < 0.0001$ by Wilcoxon matched-pairs signed rank test; **Figure 5B and Figure S2**). These results suggest that the P681R-bearing pseudovirus is relatively resistant to NAbs. In contrast to the neutralizing activity against cell-free viruses, the SARS-CoV-2 S-based fusion assay showed that cell-cell infection is strongly resistant to the NAbs and the insensitivity to the NAbs on cell-cell infection is not dependent on the P681R mutation (**Figure 5C**). Altogether, these findings suggest that the P681R mutation confers the NAbs resistance upon cell-free viral particles and cell-cell infection is resistant to the NAb-mediated antiviral action compared to cell-free infection.

Discussion

It is evident that most VOCs considered so far have acquired mutations in their S proteins, particularly in the RBD and N-terminal domain, to evade NAbs (Corti et al., 2021; Harvey et al., 2021; Piccoli et al., 2020). In sharp contrast, here we demonstrated that the B.1.617 lineage has acquired a unique strategy to facilitate infection and evade antiviral immunity. The P681R mutation that is highly conserved in this lineage enhances the efficacy to viral fusion and further accelerates its speed of action. The P681R-mediated rapid kinetics of viral fusion may attribute to not only immune evasion but also possibly feasible the infection to exposed individuals.

Consistent with previous reports (Kruglova et al., 2021; Xia et al., 2020), here we showed that the cell-cell infection mediated by the SARS-CoV-2 S protein is resistant to NAbs. The effect of NAbs against cell-cell infection has been well studied in HIV-1 (*Retroviridae*) infection, and it is well known that cell-cell infection is relatively more resistant to NAbs compared to cell-free infection [reviewed in (Agosto et al., 2015; Dufloo et al., 2018; Sattentau, 2008)]. The resistance of cell-cell spread against NAbs is not limited to HIV-1 but has been observed in the other viruses such as vaccinia virus (*Poxviridae*) (Law et al., 2002) and hepatitis C virus (*Flaviviridae*) (Timpe et al., 2008), suggesting that cell-cell infection is a common strategy for a variety of viruses to evade antiviral humoral immunity. The fact that the B.1.617 variants as well as the P681R mutant efficiently form syncytia and the S P681R mutant accelerates and promotes cell-cell fusion suggests that switching the preference of viral replication mode from cell-free infection to cell-cell infection may be a unique strategy of the B.1.617 variants to evade antiviral immunity.

Previous studies have demonstrated the close association of the FCS in the SARS-CoV-2 S protein with viral replication mode and it is dependent on TMPRSS2. Johnson et al. and Peacock et al. showed that the loss of FCS results in the increase of viral replication efficacy in Vero cells while the attenuation of viral growth in the Vero cells expressing TMPRSS2 (Johnson et al., 2021; Peacock et al., 2021). On the contrary, here we showed that the replication efficacy of the B.1.617 variants was severely decreased in Vero cells compared to VeroE6/TMPRSS2 cells. Together with previous findings, our data suggest that the furin-mediated cleavage of the SARS-CoV-2 S protein closely associates with the usage of TMPRSS2. On the other hand, both the FCS-deficient (Johnson et al., 2021) and the P681R-mutated pseudoviruses were resistant to the NAb-mediated antiviral effect. These data suggest that the resistance of the viruses harboring mutations around FCS is not dependent on the usage of TMPRSS2 and the tropism of cell-cell infection.

Although the P681R mutation is not located in the RBD of SARS-CoV-2 S protein, the P681R-harboring pseudovirus rendered resistance to the NAbs targeting

RBD. Regarding this, the similarity of the evolutionary trajectory of HIV-1 envelope (Env) protein and SARS-CoV-2 S protein has been discussed [reviewed in (Fischer et al., 2021)]. In the case of HIV-1 Env, a type of well studied anti-HIV-1 NAbs (e.g., 2G12, PGT121 and KD-247) targets the variable 3 (V3) region of Env [reviewed in (Sok and Burton, 2018). The Env V3 region is conformationally masked before the binding to viral receptor CD4 and is exposed after receptor binding to proceed viral entry step and determine the tropism of the usage of viral coreceptors [reviewed in (Arrildt et al., 2012)], suggesting that the V3 region is immunodominant and masking the immunodominant epitopes is a strategy for viruses to evade antiviral immunity. In fact, an artificially mutated HIV-1 Env that stably exposes the V3 region can be highly sensitive to the NAbs targeting the V3 region (Hoffman et al., 1999). To overcome the V3-targeting neutralization, HIV-1 Env usually acquires mutations not in the V3 region but in the regions next to the V3 and conformationally masks the epitope in the V3 region (Hatada et al., 2010; Pinter et al., 2005; Pinter et al., 2004; Shibata et al., 2007). Although most NAbs against SARS-CoV-2 target the RBD of S protein (Piccoli et al., 2020), viruses, mainly VOCs, have acquired mutations in this domain (e.g., E484K) to evade neutralization (Baum et al., 2020; Chen et al., 2021; Liu et al., 2021c; Wang et al., 2021b; Weisblum et al., 2020). On the other hand, the P681R mutation is not located in the RBD. Considering the examples of HIV-1 Env studies, the P681R mutation may conformationally mask the immunodominant epitopes located in the RBD to ablate the accessibility of NAb to this domain. Moreover, although the pseudovirus infectivity bearing the P681R mutation was ~2-fold attenuated when the TMPRSS2-expressing cells were used as the target cells, the P681R-bearing pseudovirus exhibited resistance to NAbs. Therefore, the acquisition of this mutation may be due to a trade-off between viral infectivity and immune evasion.

In summary, here we demonstrated that the P681R mutation, a hallmark of the B.1.617 lineage, enhances viral fusion and promotes cell-cell infection. Although the P681R mutant is highly fusogenic, the virus harboring the P681R mutation did not necessarily show higher growth compared to the parental virus. Regarding this, the HIV-1 variants with higher fusogenicity have been isolated from AIDS patients, but the enhanced fusogenicity does not promote viral replication in *in vitro* cell cultures (Sterjovski et al., 2007). Similarly, the measles virus (*Paramyxoviridae*) harboring the deficient mutation in viral matrix protein (Cathomen et al., 1998) and substitution mutations in viral fusion protein (Ikegame et al., 2021; Watanabe et al., 2013) are highly fusogenic and efficiently expands via cell-cell fusion. However, the growth kinetics of the mutated measles virus with higher fusogenicity in *in vitro* cell cultures is less efficient than the parental virus (Cathomen et al., 1998). Therefore,

the discrepancy between the efficacy of viral growth in *in vitro* cell cultures and viral fusogenicity is not specific for SARS-CoV-2. Rather, the higher fusogenicity is associated with the severity of viral pathogenicity such as HIV-1 encephalitis (Rossi et al., 2008) and fatal subacute sclerosing panencephalitis, which is caused by measles virus infection in brain (Ikegame et al., 2021; Watanabe et al., 2013). Although the association between the COVID-19 severity and/or unusual symptoms caused by SARS-CoV-2 infection and the P681R mutation remains unclear, an early report from the PRE suggests the B.1.617.2 variant, which bears the P681R mutation, may be more pathogenic than the B.1.1.7 lineage (PHE, 2021). Switching viral infection mode by the P681R mutation may relate to the severity and/or unusual outcome of viral infection, therefore, the epidemic of the SARS-CoV-2 variants harboring the P681R mutation should be surveyed in depth.

STAR★METHODS

Supplemental Information

Supplemental Information includes 2 figures and 4 tables and can be found with this article online at http://...

Author Contributions

A.S., H.N., K.U., Y.Kosugi, T.Irie, E.P.B., Y.L.T., R.S., K.Shimizu, T.F., R.K., T.Ikeda and K.Sato. performed the experiments.
K.Sadamasu, K.T., T.S., I.Y., H.A., M.N., and K.Y. prepared experimental materials.
J.W. and S.N. performed molecular phylogenetic analysis.
K.Shirakawa, Y.Kazuma, R.N., Y.H., and A.T.-K. collected clinical samples.
A.S., T.Irie, T.F., S.N., T.Ikeda and K.S. designed the experiments and interpreted the results.
K.S. wrote the original manuscript.
All authors reviewed and proofread the manuscript.
The Genotype to Phenotype Japan (G2P-Japan) Consortium contributed to the project administration.

Consortia

The Genotype to Phenotype Japan (G2P-Japan) Consortium: Mika Chiba, Hirotake Furihata, Haruyo Hasebe, Kazuko Kitazato, Haruko Kubo, Naoko Misawa, Nanami Morizako, Akiko Oide, Mai Suganami, Miyoko Takahashi, Kana Tsushima, Miyabishara Yokoyama, Yue Yuan

Acknowledgments

We would like to thank all members belonging to The Genotype to Phenotype Japan (G2P-Japan) Consortium. We thank Dr. Jin Gohda (The University of Tokyo, Japan) for providing reagents. An anti-HIV-1 p24 Monoclonal antibody (clone 183-H12-5C, Cat# ARP-3537) was obtained through the NIH HIV Reagent Program, NIAID, NIH (contributed by Drs. Bruce Chesebro and Kathy Wehrly). The super-computing resource was provided by Human Genome Center at The University of Tokyo and the NIG supercomputer at ROIS National Institute of Genetics.

This study was supported in part by AMED Research Program on Emerging and Re-emerging Infectious Diseases 20fk0108163 (to A.S.), 20fk0108401 (to T.F.), 21fk0108617 (to T.F.), 20fk0108146 (to K.Sato), 20fk0108270 (to K.Sato) and 20fk0108413 (to T.Ikeda, S.N. and K.Sato); AMED Research Program on HIV/AIDS 21fk0410033 (to A.S.) and 21fk0410039 (to K.Sato); AMED Japan Program for Infectious Diseases Research and Infrastructure 20wm0325009 and 21wm0325009 (to A.S.); JST A-STEP JPMJTM20SL (to T.Ikeda); JST SICORP (e-ASIA) JPMJSC20U1 (to K.Sato); JST SICORP JPMJSC21U5 (to K.Sato), JST CREST JPMJCR20H6 (to S.N.) and JPMJCR20H4 (to K.Sato); JSPS KAKENHI Grant-in-Aid for Scientific Research C 19K06382 (to A.S.), 18K07156 (to K.T.) and 21K07060 (to K.T.), Scientific Research B 18H02662 (to K.Sato) and 21H02737 (to K.Sato);

JSPS Fund for the Promotion of Joint International Research (Fostering Joint International Research) 18KK0447 (to K.Sato); JSPS Core-to-Core Program JPJSCCA20190008 (A. Advanced Research Networks) (to K.Sato); JSPS Research Fellow DC1 19J20488 (to I.K.); JSPS Leading Initiative for Excellent Young Researchers (LEADER) (to T.Ikeda); ONO Medical Research Foundation (to K.Sato); Ichiro Kanehara Foundation (to K.Sato); Lotte Foundation (to K.Sato); Mochida Memorial Foundation for Medical and Pharmaceutical Research (to K.Sato); Daiichi Sankyo Foundation of Life Science (to K.Sato); Sumitomo Foundation (to K.Sato); Uehara Foundation (to K.Sato); Takeda Science Foundation (to T.Ikeda and K.Sato); The Tokyo Biochemical Research Foundation (to K.Sato); Mitsubishi Foundation (to T.Ikeda); Shin-Nihon Foundation of Advanced Medical Research (to T.Ikeda); Tsuchiya Foundation (to T.Irie); a Grant for Joint Research Projects of the Research Institute for Microbial Diseases, Osaka University (to A.S.); an intramural grant from Kumamoto University COVID-19 Research Projects (AMABIE) (to T.Ikeda); Intercontinental Research and Educational Platform Aiming for Eradication of HIV/AIDS (to T.Ikeda); and Joint Usage/Research Center program of Institute for Frontier Life and Medical Sciences, Kyoto University (to K.Sato).

References

Agosto, L.M., Uchil, P.D., and Mothes, W. (2015). HIV cell-to-cell transmission: effects on pathogenesis and antiretroviral therapy. Trends Microbiol *23*, 289-295.

Arrildt, K.T., Joseph, S.B., and Swanstrom, R. (2012). The HIV-1 env protein: a coat of many colors. Curr HIV/AIDS Rep *9*, 52-63.

Baum, A., Fulton, B.O., Wloga, E., Copin, R., Pascal, K.E., Russo, V., Giordano, S., Lanza, K., Negron, N., Ni, M.*, et al.* (2020). Antibody cocktail to SARS-CoV-2 spike protein prevents rapid mutational escape seen with individual antibodies. Science *369*, 1014-1018.

Cathomen, T., Mrkic, B., Spehner, D., Drillien, R., Naef, R., Pavlovic, J., Aguzzi, A., Billeter, M.A., and Cattaneo, R. (1998). A matrix-less measles virus is infectious and elicits extensive cell fusion: consequences for propagation in the brain. EMBO J *17*, 3899-3908.

CDC (2021). "SARS-CoV-2 variant classifications and definitions (updated June 10, 2021)". https://www.cdc.gov/coronavirus/2019-ncov/variants/variant-info.html.

Chen, R.E., Zhang, X., Case, J.B., Winkler, E.S., Liu, Y., VanBlargan, L.A., Liu, J., Errico, J.M., Xie, X., Suryadevara, N.*, et al.* (2021). Resistance of SARS-CoV-2 variants to neutralization by monoclonal and serum-derived polyclonal antibodies. Nat Med *27*, 717-726.

Collier, D.A., De Marco, A., Ferreira, I., Meng, B., Datir, R., Walls, A.C., Kemp, S.S., Bassi, J., Pinto, D., Fregni, C.S.*, et al.* (2021). Sensitivity of SARS-CoV-2 B.1.1.7 to mRNA vaccine-elicited antibodies. Nature *593*, 136-141.

Corti, D., Purcell, L.A., Snell, G., and Veesler, D. (2021). Tackling COVID-19 with neutralizing monoclonal antibodies. Cell.

Deng, X., Garcia-Knight, M.A., Khalid, M.M., Servellita, V., Wang, C., Morris, M.K., Sotomayor-González, A., Glasner, D.R., Reyes, K.R., Gliwa, A.S.*, et al.* (2021). Transmission, infectivity, and antibody neutralization of an emerging SARS-CoV-2 variant in California carrying a L452R spike protein mutation. Cell *in press*.

Dufloo, J., Bruel, T., and Schwartz, O. (2018). HIV-1 cell-to-cell transmission and broadly neutralizing antibodies. Retrovirology *15*, 51.

Edara, V.-V., Lai, L., Sahoo, M.K., Floyd, K., Sibai, M., Solis, D., Flowers, M.W., Hussaini, L., Ciric, C.R., Bechnack, S.*, et al.* (2021). Infection and vaccine-induced neutralizing antibody responses to the SARS-CoV-2 B.1.617.1 variant. BioRxiv, 443299.

Ferreira, I., Datir, R., Kemp, S., Papa, G., Rakshit, P., Singh, S., Meng, B., Pandey, R., Ponnusamy, K., Radhakrishnan, V.S.*, et al.* (2021). SARS-CoV-2 B.1.617 emergence and sensitivity to vaccine-elicited antibodies. BioRxiv, 443253.

Fischer, W., Giorgi, E.E., Chakraborty, S., Nguyen, K., Bhattarcharya, T., Theiler, J.,

Goloboff, P.A., Yoon, H., Abfalterer, W., Foley, B.T., *et al.* (2021). HIV-1 and SARS-CoV-2: patterns in the evolution of two pandemic pathogens. Cell Host Microbe *pre-proof*.

Garcia-Beltran, W.F., Lam, E.C., St Denis, K., Nitido, A.D., Garcia, Z.H., Hauser, B.M., Feldman, J., Pavlovic, M.N., Gregory, D.J., Poznansky, M.C., *et al.* (2021). Multiple SARS-CoV-2 variants escape neutralization by vaccine-induced humoral immunity. Cell *184*, 2372-2383 e2379.

Harvey, W.T., Carabelli, A.M., Jackson, B., Gupta, R.K., Thomson, E.C., Harrison, E.M., Ludden, C., Reeve, R., Rambaut, A., Consortium, C.-G.U., *et al.* (2021). SARS-CoV-2 variants, spike mutations and immune escape. Nat Rev Microbiol.

Hatada, M., Yoshimura, K., Harada, S., Kawanami, Y., Shibata, J., and Matsushita, S. (2010). Human immunodeficiency virus type 1 evasion of a neutralizing anti-V3 antibody involves acquisition of a potential glycosylation site in V2. J Gen Virol *91*, 1335-1345.

Hoffman, T.L., LaBranche, C.C., Zhang, W., Canziani, G., Robinson, J., Chaiken, I., Hoxie, J.A., and Doms, R.W. (1999). Stable exposure of the coreceptor-binding site in a CD4-independent HIV-1 envelope protein. Proc Natl Acad Sci U S A *96*, 6359-6364.

Hoffmann, M., Arora, P., Gross, R., Seidel, A., Hornich, B.F., Hahn, A.S., Kruger, N., Graichen, L., Hofmann-Winkler, H., Kempf, A., *et al.* (2021). SARS-CoV-2 variants B.1.351 and P.1 escape from neutralizing antibodies. Cell *184*, 2384-2393 e2312.

Hou, Y.J., Chiba, S., Halfmann, P., Ehre, C., Kuroda, M., Dinnon, K.H., 3rd, Leist, S.R., Schafer, A., Nakajima, N., Takahashi, K., *et al.* (2020). SARS-CoV-2 D614G variant exhibits efficient replication ex vivo and transmission in vivo. Science *370*, 1464-1468.

Ikeda, T., Molan, A.M., Jarvis, M.C., Carpenter, M.A., Salamango, D.J., Brown, W.L., and Harris, R.S. (2019). HIV-1 restriction by endogenous APOBEC3G in the myeloid cell line THP-1. J Gen Virol *100*, 1140-1152.

Ikeda, T., Symeonides, M., Albin, J.S., Li, M., Thali, M., and Harris, R.S. (2018). HIV-1 adaptation studies reveal a novel Env-mediated homeostasis mechanism for evading lethal hypermutation by APOBEC3G. PLoS Pathog *14*, e1007010.

Ikegame, S., Hashiguchi, T., Hung, C.T., Dobrindt, K., Brennand, K.J., Takeda, M., and Lee, B. (2021). Fitness selection of hyperfusogenic measles virus F proteins associated with neuropathogenic phenotypes. Proc Natl Acad Sci U S A *118*.

Johnson, B.A., Xie, X., Bailey, A.L., Kalveram, B., Lokugamage, K.G., Muruato, A., Zou, J., Zhang, X., Juelich, T., Smith, J.K., *et al.* (2021). Loss of furin cleavage site attenuates SARS-CoV-2 pathogenesis. Nature *591*, 293-299.

Katoh, K., and Standley, D.M. (2013). MAFFT multiple sequence alignment software

version 7: improvements in performance and usability. Mol Biol Evol *30*, 772-780.

Kawase, M., Shirato, K., van der Hoek, L., Taguchi, F., and Matsuyama, S. (2012). Simultaneous treatment of human bronchial epithelial cells with serine and cysteine protease inhibitors prevents severe acute respiratory syndrome coronavirus entry. J Virol *86*, 6537-6545.

Kondo, N., Miyauchi, K., and Matsuda, Z. (2011). Monitoring viral-mediated membrane fusion using fluorescent reporter methods. Curr Protoc Cell Biol *Chapter 26*, Unit 26 29.

Korber, B., Fischer, W.M., Gnanakaran, S., Yoon, H., Theiler, J., Abfalterer, W., Hengartner, N., Giorgi, E.E., Bhattacharya, T., Foley, B.*, et al.* (2020). Tracking changes in SARS-CoV-2 spike: evidence that D614G increases infectivity of the COVID-19 virus. Cell *182*, 812-827.

Kruglova, N., Siniavin, A., Gushchin, V., and Mazurov, D. (2021). SARS-CoV-2 cell-to-cell infection is resistant to neutralizing antibodies. BioRxiv, 442701.

Law, M., Hollinshead, R., and Smith, G.L. (2002). Antibody-sensitive and antibody-resistant cell-to-cell spread by vaccinia virus: role of the A33R protein in antibody-resistant spread. J Gen Virol *83*, 209-222.

Liu, J., Liu, Y., Xia, H., Zou, J., Weaver, S.C., Swanson, K.A., Cai, H., Cutler, M., Cooper, D., Muik, A.*, et al.* (2021a). BNT162b2-elicited neutralization of B.1.617 and other SARS-CoV-2 variants. Nature *accelerated*.

Liu, Y., Liu, J., Xia, H., Zhang, X., Fontes-Garfias, C.R., Swanson, K.A., Cai, H., Sarkar, R., Chen, W., Cutler, M.*, et al.* (2021b). Neutralizing activity of BNT162b2-elicited serum. N Engl J Med *384*, 1466-1468.

Liu, Z., VanBlargan, L.A., Bloyet, L.M., Rothlauf, P.W., Chen, R.E., Stumpf, S., Zhao, H., Errico, J.M., Theel, E.S., Liebeskind, M.J.*, et al.* (2021c). Identification of SARS-CoV-2 spike mutations that attenuate monoclonal and serum antibody neutralization. Cell Host Microbe *29*, 477-488 e474.

Matsuyama, S., Nao, N., Shirato, K., Kawase, M., Saito, S., Takayama, I., Nagata, N., Sekizuka, T., Katoh, H., Kato, F.*, et al.* (2020). Enhanced isolation of SARS-CoV-2 by TMPRSS2-expressing cells. Proc Natl Acad Sci U S A *117*, 7001-7003.

Minh, B.Q., Schmidt, H.A., Chernomor, O., Schrempf, D., Woodhams, M.D., von Haeseler, A., and Lanfear, R. (2020). IQ-TREE 2: New Models and Efficient Methods for Phylogenetic Inference in the Genomic Era. Mol Biol Evol *37*, 1530-1534.

Motozono, C., Toyoda, M., Zahradnik, J., Ikeda, T., Saito, A., Tan, T.S., Ngare, I., Nasser, H., Kimura, I., Uriu, K.*, et al.* (2021). An emerging SARS-CoV-2 mutant evading cellular immunity and increasing viral infectivity. BioRxiv, 438288.

Niwa, H., Yamamura, K., and Miyazaki, J. (1991). Efficient selection for high-expression transfectants with a novel eukaryotic vector. Gene *108*, 193-199.

563 Ozono, S., Zhang, Y., Ode, H., Sano, K., Tan, T.S., Imai, K., Miyoshi, K., Kishigami,
564 S., Ueno, T., Iwatani, Y.*, et al.* (2021). SARS-CoV-2 D614G spike mutation increases
565 entry efficiency with enhanced ACE2-binding affinity. Nat Commun *12*, 848.
566 Ozono, S., Zhang, Y., Tobiume, M., Kishigami, S., and Tokunaga, K. (2020). Super-
567 rapid quantitation of the production of HIV-1 harboring a luminescent peptide tag. J
568 Biol Chem *295*, 13023-13030.
569 Peacock, T.P., Goldhill, D.H., Zhou, J., Baillon, L., Frise, R., Swann, O.C.,
570 Kugathasan, R., Penn, R., Brown, J.C., Sanchez-David, R.Y.*, et al.* (2021). The furin
571 cleavage site in the SARS-CoV-2 spike protein is required for transmission in ferrets.
572 Nat Microbiol.
573 PHE (2021). Public Health England. "3 June 2021 Risk assessment for SARS-CoV-
574 2 variant: Delta (VOC-21APR-02, B.1.617.2)"
575 https://assets.publishing.service.gov.uk/government/uploads/system/uploads/attac
576 hment_data/file/991135/3_June_2021_Risk_assessment_for_SARS-CoV-
577 2_variant_DELTA.pdf.
578 Piccoli, L., Park, Y.J., Tortorici, M.A., Czudnochowski, N., Walls, A.C., Beltramello,
579 M., Silacci-Fregni, C., Pinto, D., Rosen, L.E., Bowen, J.E.*, et al.* (2020). Mapping
580 Neutralizing and Immunodominant Sites on the SARS-CoV-2 Spike Receptor-
581 Binding Domain by Structure-Guided High-Resolution Serology. Cell *183*, 1024-
582 1042 e1021.
583 Pinter, A., Honnen, W.J., D'Agostino, P., Gorny, M.K., Zolla-Pazner, S., and Kayman,
584 S.C. (2005). The C108g epitope in the V2 domain of gp120 functions as a potent
585 neutralization target when introduced into envelope proteins derived from human
586 immunodeficiency virus type 1 primary isolates. J Virol *79*, 6909-6917.
587 Pinter, A., Honnen, W.J., He, Y., Gorny, M.K., Zolla-Pazner, S., and Kayman, S.C.
588 (2004). The V1/V2 domain of gp120 is a global regulator of the sensitivity of primary
589 human immunodeficiency virus type 1 isolates to neutralization by antibodies
590 commonly induced upon infection. J Virol *78*, 5205-5215.
591 Planas, D., Bruel, T., Grzelak, L., Guivel-Benhassine, F., Staropoli, I., Porrot, F.,
592 Planchais, C., Buchrieser, J., Rajah, M.M., Bishop, E.*, et al.* (2021). Sensitivity of
593 infectious SARS-CoV-2 B.1.1.7 and B.1.351 variants to neutralizing antibodies. Nat
594 Med *27*, 917-924.
595 Plante, J.A., Liu, Y., Liu, J., Xia, H., Johnson, B.A., Lokugamage, K.G., Zhang, X.,
596 Muruato, A.E., Zou, J., Fontes-Garfias, C.R.*, et al.* (2020). Spike mutation D614G
597 alters SARS-CoV-2 fitness. Nature.
598 Plante, J.A., Mitchell, B.M., Plante, K.S., Debbink, K., Weaver, S.C., and Menachery,
599 V.D. (2021). The variant gambit: COVID's next move. Cell Host Microbe *29*, 508-
600 515.

Rausch, T., Fritz, M.H., Untergasser, A., and Benes, V. (2020). Tracy: basecalling, alignment, assembly and deconvolution of sanger chromatogram trace files. BMC Genomics *21*, 230.

Reed, L.J., and Muench, H. (1938). A Simple Method of Estimating Fifty Percent Endpoints. Am J Hygiene *27*, 493-497.

Rossi, F., Querido, B., Nimmagadda, M., Cocklin, S., Navas-Martin, S., and Martin-Garcia, J. (2008). The V1-V3 region of a brain-derived HIV-1 envelope glycoprotein determines macrophage tropism, low CD4 dependence, increased fusogenicity and altered sensitivity to entry inhibitors. Retrovirology *5*, 89.

Sattentau, Q. (2008). Avoiding the void: cell-to-cell spread of human viruses. Nat Rev Microbiol *6*, 815-826.

Shang, J., Wan, Y., Luo, C., Ye, G., Geng, Q., Auerbach, A., and Li, F. (2020). Cell entry mechanisms of SARS-CoV-2. Proc Natl Acad Sci U S A *117*, 11727-11734.

Shema Mugisha, C., Vuong, H.R., Puray-Chavez, M., Bailey, A.L., Fox, J.M., Chen, R.E., Wessel, A.W., Scott, J.M., Harastani, H.H., Boon, A.C.M.*, et al.* (2020). A simplified quantitative real-time PCR assay for monitoring SARS-CoV-2 growth in cell culture. mSphere *5*.

Shibata, J., Yoshimura, K., Honda, A., Koito, A., Murakami, T., and Matsushita, S. (2007). Impact of V2 mutations on escape from a potent neutralizing anti-V3 monoclonal antibody during in vitro selection of a primary human immunodeficiency virus type 1 isolate. J Virol *81*, 3757-3768.

Singh, J., Rahman, S.A., Ehtesham, N.Z., Hira, S., and Hasnain, S.E. (2021). SARS-CoV-2 variants of concern are emerging in India. Nat Med.

Sok, D., and Burton, D.R. (2018). Recent progress in broadly neutralizing antibodies to HIV. Nat Immunol *19*, 1179-1188.

Sterjovski, J., Churchill, M.J., Ellett, A., Gray, L.R., Roche, M.J., Dunfee, R.L., Purcell, D.F., Saksena, N., Wang, B., Sonza, S.*, et al.* (2007). Asn 362 in gp120 contributes to enhanced fusogenicity by CCR5-restricted HIV-1 envelope glycoprotein variants from patients with AIDS. Retrovirology *4*, 89.

Sultana, T., Mamede, J.I., Saito, A., Ode, H., Nohata, K., Cohen, R., Nakayama, E.E., Iwatani, Y., Yamashita, M., Hope, T.J.*, et al.* (2019). Multiple Pathways To Avoid Beta Interferon Sensitivity of HIV-1 by Mutations in Capsid. J Virol *93*.

Timpe, J.M., Stamataki, Z., Jennings, A., Hu, K., Farquhar, M.J., Harris, H.J., Schwarz, A., Desombere, I., Roels, G.L., Balfe, P.*, et al.* (2008). Hepatitis C virus cell-cell transmission in hepatoma cells in the presence of neutralizing antibodies. Hepatology *47*, 17-24.

Torii, S., Ono, C., Suzuki, R., Morioka, Y., Anzai, I., Fauzyah, Y., Maeda, Y., Kamitani, W., Fukuhara, T., and Matsuura, Y. (2021). Establishment of a reverse genetics

system for SARS-CoV-2 using circular polymerase extension reaction. Cell Rep *35*, 109014.

Volz, E., Hill, V., McCrone, J.T., Price, A., Jorgensen, D., O'Toole, A., Southgate, J., Johnson, R., Jackson, B., Nascimento, F.F.*, et al.* (2021). Evaluating the effects of SARS-CoV-2 spike mutation D614G on transmissibility and pathogenicity. Cell *184*, 64-75 e11.

Wall, E.C., Wu, M., Harvey, R., Kelly, G., Warchal, S., Sawyer, C., Daniels, R., Hobson, P., Hatipoglu, E., Ngai, Y.*, et al.* (2021). Neutralising antibody activity against SARS-CoV-2 VOCs B.1.617.2 and B.1.351 by BNT162b2 vaccination. Lancet.

Wang, P., Casner, R.G., Nair, M.S., Wang, M., Yu, J., Cerutti, G., Liu, L., Kwong, P.D., Huang, Y., Shapiro, L.*, et al.* (2021a). Increased resistance of SARS-CoV-2 variant P.1 to antibody neutralization. Cell Host Microbe *29*, 747-751 e744.

Wang, P., Nair, M.S., Liu, L., Iketani, S., Luo, Y., Guo, Y., Wang, M., Yu, J., Zhang, B., Kwong, P.D.*, et al.* (2021b). Antibody resistance of SARS-CoV-2 variants B.1.351 and B.1.1.7. Nature *593*, 130-135.

Watanabe, S., Shirogane, Y., Suzuki, S.O., Ikegame, S., Koga, R., and Yanagi, Y. (2013). Mutant fusion proteins with enhanced fusion activity promote measles virus spread in human neuronal cells and brains of suckling hamsters. J Virol *87*, 2648-2659.

Weisblum, Y., Schmidt, F., Zhang, F., DaSilva, J., Poston, D., Lorenzi, J.C., Muecksch, F., Rutkowska, M., Hoffmann, H.H., Michailidis, E.*, et al.* (2020). Escape from neutralizing antibodies by SARS-CoV-2 spike protein variants. Elife *9*.

WHO (2021a). "Coronavirus disease 2019". https://www.who.int/emergencies/diseases/novel-coronavirus-2019.

WHO (2021b). "Tracking SARS-CoV-2 variants". https://www.who.int/en/activities/tracking-SARS-CoV-2-variants/.

Wu, F., Zhao, S., Yu, B., Chen, Y.M., Wang, W., Song, Z.G., Hu, Y., Tao, Z.W., Tian, J.H., Pei, Y.Y.*, et al.* (2020). A new coronavirus associated with human respiratory disease in China. Nature *579*, 265-269.

Xia, S., Liu, M., Wang, C., Xu, W., Lan, Q., Feng, S., Qi, F., Bao, L., Du, L., Liu, S.*, et al.* (2020). Inhibition of SARS-CoV-2 (previously 2019-nCoV) infection by a highly potent pan-coronavirus fusion inhibitor targeting its spike protein that harbors a high capacity to mediate membrane fusion. Cell Res *30*, 343-355.

Yurkovetskiy, L., Wang, X., Pascal, K.E., Tomkins-Tinch, C., Nyalile, T.P., Wang, Y., Baum, A., Diehl, W.E., Dauphin, A., Carbone, C.*, et al.* (2020). Structural and functional analysis of the D614G SARS-CoV-2 spike protein variant. Cell *183*, 739-751 e738.

677 Zhou, B., Thi Nhu Thao, T., Hoffmann, D., Taddeo, A., Ebert, N., Labroussaa, F.,
678 Pohlmann, A., King, J., Steiner, S., Kelly, J.N.*, et al.* (2021). SARS-CoV-2 spike
679 D614G change enhances replication and transmission. Nature *592*, 122-127.
680 Zhou, P., Yang, X.L., Wang, X.G., Hu, B., Zhang, L., Zhang, W., Si, H.R., Zhu, Y.,
681 Li, B., Huang, C.L.*, et al.* (2020). A pneumonia outbreak associated with a new
682 coronavirus of probable bat origin. Nature *579*, 270-273.
683

Figures

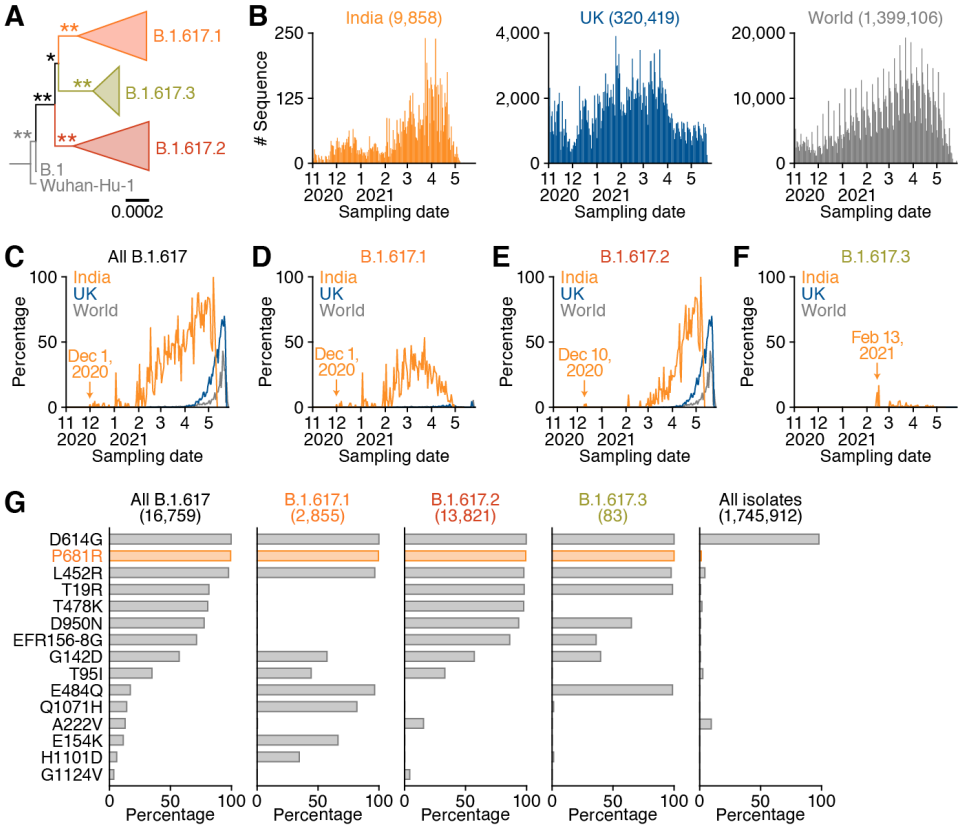

Figure 1. Molecular phylogenetic and epidemic dynamics of the B.1.617 lineage during the pandemic

(**A**) A phylogenetic tree of the B.1.617 lineage. Bar, 0.0002 substitutions per site. Bootstrap values, **, 100%; *, >70%. The uncollapsed tree is shown in **Figure S1**.

(**B-F**) Epidemic dynamics of the B.1.617 lineage. (**B**) The numbers of sequences deposited in GISAID per day for India (orange, left), UK (blue, middle), and the whole world (gray, right). (**C-F**) The percentages of each lineage deposited per day (**C**, all B.1.617; **D**, B.1.617.1; **E**, B.1.617.2; **F**, B.1.617.3) from India (orange), the UK (blue) and the whole world (gray) are shown. The date first identified is indicated. The raw data are summarized in **Table S1**.

(**G**) Proportion of amino acid replacements in the B.1.617 lineage. The top 15 replacements conserved in the S protein of the B.1.617 and its sublineages are summarized. The number in parenthesis indicates the number of sequences included in each panel. The raw data are summarized in **Table S2**.

See also **Figure S1** and **Tables S1 and S2**.

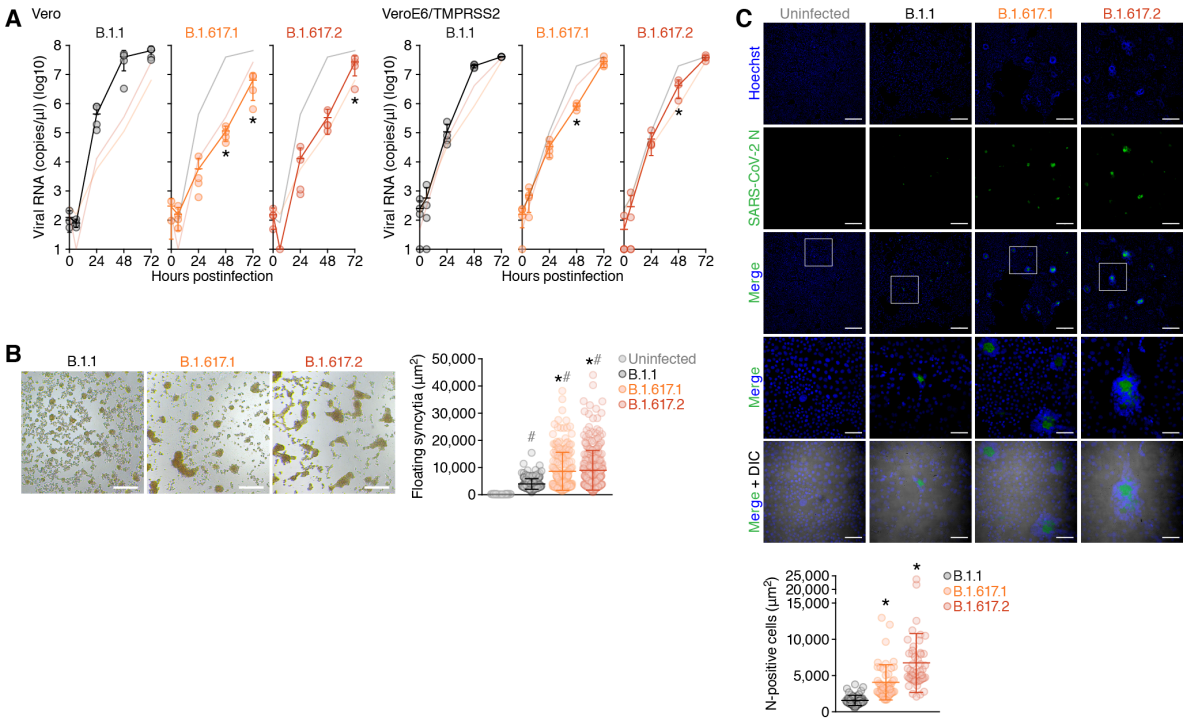

Figure 2. Virological features of the B.1.617 lineage

(**A**) Growth kinetics of two B.1.617 variants and a B.1.1 isolate. Two viral isolates of B.1.617.1 (GISAID ID: EPI_ISL_2378733) and B.1.617.2 (GISAID ID: EPI_ISL_2378732) and a D614G-bearing B.1.1 isolate (GISAID ID: EPI_ISL_479681) [100 50% tissue culture infectious dose ($TCID_{50}$)] were inoculated into Vero cells, VeroE6/TMPRSS2 cells and the copy number of viral RNA in the culture supernatant was quantified by real-time RT-PCR. The growth curves of the viruses inoculated are shown. Assays were performed in quadruplicate.

(**B**) Syncytia formation. The syncytia in infected VeroE6/TMPRSS2 cells were observed at 72 hours postinfection (hpi). (Left) Representative bright-field images of VeroE6/TMPRSS2 cells at 72 hpi are shown. Bars, 100 μm. (Right) The size of floating syncytia in B.1.1-infected (n = 217), B.1.617.1-infected (n = 306) and B.1.617.2-infected (n = 217) cultures are shown. The size of the floating single cells in uninfected culture (n = 177) was also shown as a negative control.

(**C**) Immunofluorescence staining. VeroE6/TMPRSS2 cells infected with the viruses indicated [multiplicity of infection (MOI) 0.01] were stained with anti-SARS-CoV-2 nucleocapsid (N) (green) and DAPI (blue). (Top) Representative images at 48 hpi are shown. Areas enclosed with squares are enlarged in the bottom panels. DIC, differential interference contrast. Bars, 200 μm for low magnification panels; 50 μm for high magnification panels. (Bottom) The area of N-positive cells in B.1.1-infected (n = 50), B.1.617.1-infected (n = 50) and B.1.617.2-infected (n = 50) cultures are shown.

725 In **A**, statistically significant differences (*, $P < 0.05$) versus the B.1.1 isolate were
726 determined by Student's *t* test.
727 In **B and C**, statistically significant differences versus the B.1.1-infected culture (*, P
728 < 0.05) and uninfected culture (#, $P < 0.05$) were determined by the Mann-Whitney
729 U test.

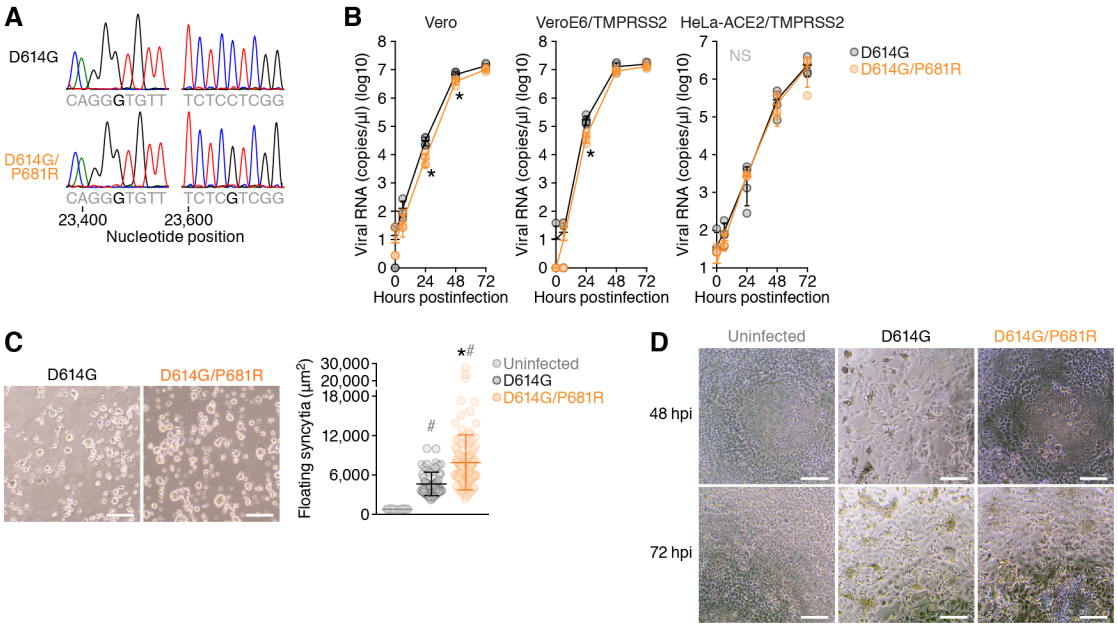

Figure 3. Virological features of the P681R-harboring virus

(**A**) Chromatograms of the mutated regions of SARS-CoV-2 viruses artificially generated by reverse genetics. Chromatograms of nucleotide positions 23,399-23,407 (left) and 23,600-23,609 (right) of parental SARS-CoV-2 (strain WK-521, PANGO lineage A; GISAID ID: EPI_ISL_408667) and the D614G (A23403G in nucleotide) and P681R (C23604G in nucleotide) mutation are shown.

(**B**) Growth kinetics of artificially generated viruses. The D614G and D614G/P681R mutant viruses were generated by reverse genetics. These viruses (100 $TCID_{50}$) were inoculated into Vero cells, VeroE6/TMPRSS2 cells, and HeLa-ACE2/TMPRSS2 cells and the copy number of viral RNA in the culture supernatant was quantified by real-time RT-PCR. The growth curves of the viruses inoculated are shown. Assays were performed in quadruplicate.

(**C and D**) Syncytia formation. The floating syncytia in infected VeroE6/TMPRSS2 cells at 72 hpi (**C**) and the adherent syncytia in infected HeLa-ACE2/TMPRSS2 at 48 hpi (**D**) are shown. In **C**, The size of floating syncytia in the D614G mutant-infected (n = 63) and the D614G/P681R mutant-infected (n = 126) cultures are shown. The size of the floating single cells in uninfected culture (n = 60) was also shown as a negative control. Bars, 100 μm.

In **B**, statistically significant differences (*, $P < 0.05$) versus the D614G virus were determined by Student's *t* test.

In **C**, statistically significant differences versus the D614G mutant-infected culture (*, $P < 0.05$) and uninfected culture (#, $P < 0.05$) were determined by the Mann-Whitney U test.

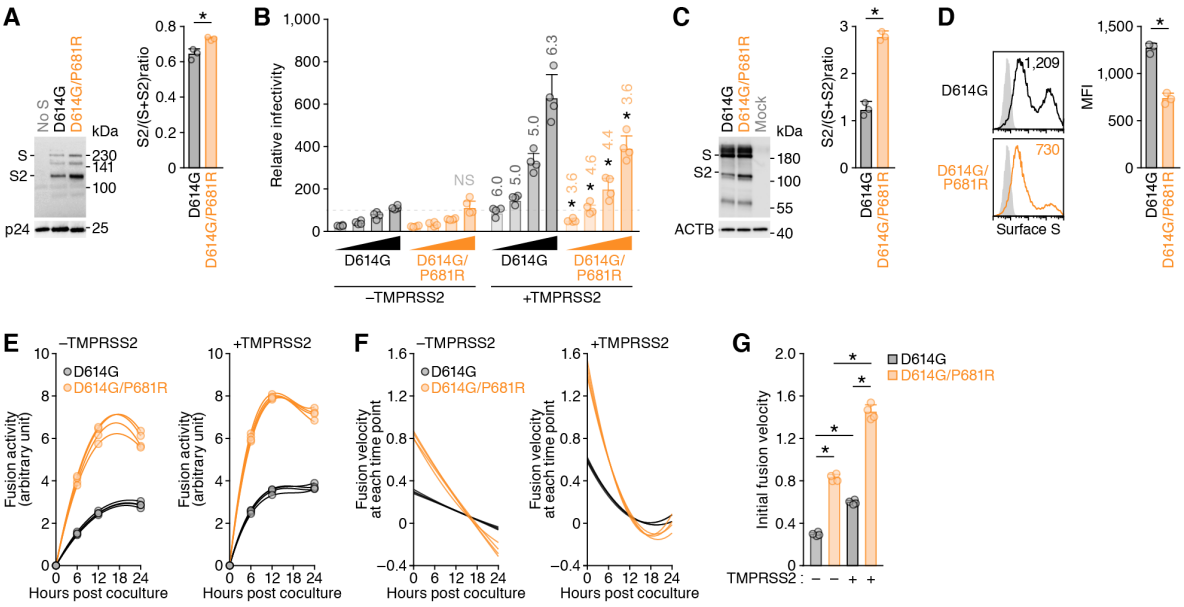

Figure 4. Promotion of cell-cell fusion by the P681R mutation

(**A**) Western blotting of pseudoviruses. (Left) Representative blots of SARS-CoV-2 full-length S and cleaved S2 proteins as well as HIV-1 p24 capsid as an internal control. kDa, kilodalton. (Right) The ratio of S2 to the full-length S plus S2 proteins on pseudovirus particles.

(**B**) Pseudovirus assay. The HIV-1-based reporter virus pseudotyped with the SARS-CoV-2 S D614G or D614G/P681R was inoculated into HOS-ACE2 cells or HOS-ACE2/TMPRSS2 cells at 4 different doses (2.5×10^5, 5.0×10^5, 1×10^6 and 2×10^6 HiBiT values). Percentages of infectivity compared to the virus pseudotyped with parental S D614G (2×10^6 HiBiT values) in HOS-ACE2 cells are shown. The numbers on the bars of the HOS-ACE2/TMPRSS2 cell data indicate the fold change versus the HOS-ACE2 cell data. Assays were performed in quadruplicate.

(**C**) Western blotting of the S-expressing cells. (Left) Representative blots of SARS-CoV-2 full-length S and cleaved S2 proteins as well as ACTB as an internal control. kDa, kilodalton. (Right) The ratio of S2 to the full-length S plus S2 proteins in the S-expressing cells.

(**D**) Flow cytometry of the S-expressing cells. (Left) Representative histogram of the S protein expression on the cell surface. The number in the histogram indicates the mean fluorescence intensity (MFI). (Right) The MFI of surface S on the S-expressing cells.

(**E-G**) SARS-CoV-2 S-based fusion assay. Effector cells (S-expressing cells) and target cells (ACE2-expressing cells or ACE2/TMPRSS2-expressing cells) were prepared, and the fusion activity was measured as described in **STAR★METHODS**.

(**E**) Kinetics of fusion activity (experimental data). Assays were performed in

779 quadruplicate, and fusion activity (arbitrary unit) is shown. (**F and G**) The kinetics
780 of fusion velocity estimated by a mathematical model based on the kinetics of fusion
781 activity data (see **STAR★METHODS**). (**G**) Initial velocity of the S-mediated fusion.
782 In **B, D, and E**, statistically significant differences (*, $P < 0.05$) versus the D614G S
783 were determined by Student's *t* test.
784 In **F and G,** statistically significant differences (*, $P < 0.05$) versus the D614G S were
785 determined by two-sided Welch's *t* test.

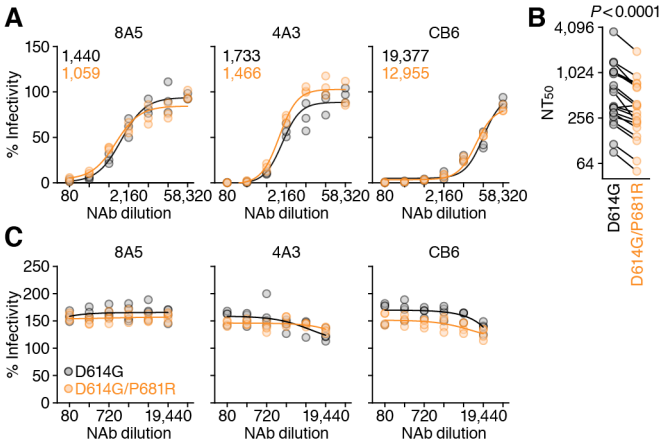

Figure 5. Association of the P681R mutation on the sensitivity to NAbs

Neutralization assay was performed by using three RBD-targeting monoclonal antibodies (clones 8A5, 4A3 and CB6) (**A and C**) and 19 vaccinated sera (**B**). NAbs were used for the pseudovirus assay (**A and B**) and the S-based fusion assay (**C**). Pseudoviruses and effector cells (S-expressing cells) were treated with serially diluted NAbs or sera as described in **STAR★METHODS**. The raw data of **B** is shown in **Figure S2**. NT_{50}, 50% neutralization titer.

In **A**, the NT_{50} values of the D614G S (black) and D614G/P681R S (orange) are indicated.

In **B**, a statistically significant difference versus the D614G virus was determined by Wilcoxon matched-pairs signed rank test.

See also **Figure S2**.

Table S1. Number of daily deposited sequences in GISAID, related to Figure 1

Table S2. Percentage of the mutations detected in the S protein of the B.1.617 lineage, related to Figure 1

Table S3. The SARS-CoV-2 genomic region encoded by each template and the primers used for the preparation of each fragment for CPER, related to Figure 2

Table S4. Primers used for the preparation of the expression plasmids for mutated SARS-CoV-2 S proteins, related to Figure 4

STAR★METHODS

KEY RESOURCES TABLE

RESOURCE AVAILABILITY

Lead Contact

Further information and requests for resources and reagents should be directed to and will be fulfilled by the Lead Contact, Kei Sato (KeiSato@g.ecc.u-tokyo.ac.jp).

Materials Availability

All unique reagents generated in this study are listed in the Key Resources Table and available from the Lead Contact with a completed Materials Transfer Agreement.

Data and Code Availability

Additional Supplemental Items are available from Mendeley Data at http://...

EXPERIMENTAL MODEL AND SUBJECT DETAILS

Ethics Statement

For virus isolation, this study was approved by the Institutional Review Board of Tokyo Metropolitan Institute of Public Health, according to the Declaration of Helsinki 2013 (approval number 3KenKenKen-466). For the use of human specimen, all protocols involving human subjects recruited at Kyoto University were reviewed and approved by the Institutional Review Boards of Kyoto University (approval number G0697). All human subjects provided written informed consent.

Collection of BNT162b2-Vaccinated Sera

Peripheral blood were collected four weeks after the second vaccination of BNT162b2 (Pfizer-BioNTech), and the sera of 19 vaccinees (average age: 38, range: 28-59, 26% male) were isolated from peripheral blood. Sera were inactivated at 56°C for 30 min and stored at –80°C until use.

Cell Culture

HEK293 cells (a human embryonic kidney cell line; ATCC CRL-1573), HEK293T cells (a human embryonic kidney cell line; ATCC CRL-3216), and HOS cells (a human osteosarcoma cell line; ATCC CRL-1543) were maintained in Dulbecco's modified Eagle's medium (high glucose) (Wako, Cat# 044-29765) containing 10% fetal bovine serum (FBS) and 1% PS.

HOS-ACE2/TMPRSS2 cells, the HOS cells stably expressing human ACE2, was prepared as described previously (Ferreira et al., 2021; Ozono et al., 2021).
Vero cells [an African green monkey (*Chlorocebus sabaeus*) kidney cell line; JCRB0111] were maintained in Eagle's minimum essential medium (Wako, Cat# 051-07615) containing 10% FBS and 1% PS.
VeroE6/TMPRSS2 cells [an African green monkey (*Chlorocebus sabaeus*) kidney cell line; JCRB1819] (Matsuyama et al., 2020) were maintained in Dulbecco's modified Eagle's medium (low glucose) (Wako, Cat# 041-29775) containing 10% FBS, G418 (1 mg/ml; Nacalai Tesque, Cat# G8168-10ML) and 1% PS.
HeLa-ACE2-TMPRSS2 cells (JCRB1835 (Kawase et al., 2012) were maintained in Dulbecco's modified Eagle's medium (low glucose) (Sigma-Aldrich, Cat# D6046-500ML) containing 10% FBS, 1 mg/ml G418 and 1% PS.
HEK293-C34 cells, the *IFNAR1* KO HEK293 cells expressing human ACE2 and TMPRSS2 by doxycycline treatment (Torii et al., 2021), were maintained in Dulbecco's modified Eagle's medium (high glucose) (Sigma-Aldrich, Cat# R8758-500ML) containing 10% FBS, 10 µg/ml blasticidin (InvivoGen, Cat# ant-bl-1) and 1% PS.

METHOD DETAILS

Viral Genomes

All SARS-CoV-2 genome sequences and annotation information used in this study were downloaded from GISAID (https://www.gisaid.org) as of May 31, 2021 (1,761,037 sequences). We first excluded the genomes with non-human hosts. We obtained SARS-CoV-2 variants belonging to the B.1.617 lineage based on the PANGO annotation (i.e. sublineages B.1.617.1, B.1.617.2, or B.1.617.3) for each sequence in the GISAID metadata. Note that only one variant belonging to the B.1.617 lineage (GISAID ID: EPI_ISL_1544002 isolated in India on February 25, 2021) was not used in the analysis because the variant is not assigned any three sublineages possibly due to 212 undetermined nucleotides in the genome. To infer epidemiology of the B.1.617 lineage (**Figure 1B-1F**), we excluded genomes that sampling date information are not available, and collected 2,855, 13,821, or 83 sequences belonging to the B.1.617.1, B.1.617.2, or B.1.617.3 sublineage, respectively.

Phylogenetic Analyses

To infer the phylogeny of the B.1.617 sublineages, we screened SARS-CoV-2 genomes by removing genomes containing undetermined nucleotides at coding regions. Since the number of genomes belonging to the sublineage B.1.617.1 or

884 B.1.617.2 are large (i.e. 894 or 6152 sequences, respectively), we used 150
885 sequences randomly chosen for each sublineage. For the B.1.617.3 sublineage, 32
886 genomes were used. We used Wuhan-Hu-1 strain isolated in China on December
887 31, 2019 (GenBank ID: NC_045512.2 and GISAID ID: EPI_ISL_402125) and LOM-
888 ASST-CDG1 strain isolated Italy on February 20, 2020 (GISAID ID:
889 EPI_ISL_412973) as an outgroup. We then collected 334 representative SARS-
890 CoV-2 sequences, and aligned entire genome sequences by using the FFT-NS-1
891 program in MAFFT suite v7.407 (Katoh and Standley, 2013). All sites with gaps in
892 alignment are removed, and the total length of alignment is 29,085 nucleotides.
893 Maximum likelihood tree was generated by IQ-TREE 2 v2.1.3 software with 1,000
894 bootstraps (Minh et al., 2020). GTR+G substitution model is utilized based on BIC
895 criterion.
896
897 **SARS-CoV-2 Preparation and Titration**
898 Two viral isolates belonging to the B.1.617 lineage, B.1.617.1 (GISAID ID:
899 EPI_ISL_2378733) and B.1.617.2 (GISAID ID: EPI_ISL_2378732) and a D614G-
900 bearing B.1.1 isolate (GISAID ID: EPI_ISL_479681) were isolated from SARS-CoV-
901 2-positive individuals in Japan. Briefly, 100 µl of the nasopharyngeal swab obtained
902 from SARS-CoV-2-positive individuals were inoculated into VeroE6/TMPRSS2 cells
903 in the biosafety level 3 laboratory. After the incubation at 37°C for 15 minutes, a
904 maintenance medium supplemented with Eagle's minimum essential medium
905 (FUJIFILM Wako Pure Chemical Corporation, Cat# 056-08385) including 2% FBS
906 and 1% PS was added, and the cells were cultured at 37°C under 5% CO_2. The
907 cytopathic effect (CPE) was confirmed under an inverted microscope (Nikon), and
908 the viral load of the culture supernatant in which CPE was observed was confirmed
909 by real-time RT-PCR. To determine viral genome sequences, RNA was extracted
910 from the culture supernatant using QIAamp viral RNA mini kit (Qiagen, Qiagen, Cat#
911 52906) . cDNA library was prepared by using NEB Next Ultra RNA Library Prep Kit
912 for Illumina (New England Biolab, Cat# E7530) and whole genome sequencing was
913 performed by MiSeq (Illumina).
914 To prepare the working virus, 100 µl of the seed virus was inoculated into
915 VeroE6/TMPRSS2 cells (5,000,000 cells in a T-75 flask). At one hour after infection,
916 the culture medium was replaced with Dulbecco's modified Eagle's medium (low
917 glucose) (Wako, Cat# 041-29775) containing 2% FBS and 1% PS; at 2-3 days
918 postinfection, the culture medium was harvested and centrifuged, and the
919 supernatants were collected as the working virus.
920 The titer of the prepared working virus was measured as 50% tissue culture
921 infectious dose ($TCID_{50}$). Briefly, one day prior to infection, VeroE6/TMPRSS2 cells

(10,000 cells/well) were seeded into a 96-well plate. Serially diluted virus stocks were inoculated to the cells and incubated at 37°C for 3 days. The cells were observed under microscopy to judge the CPE appearance. The value of $TCID_{50}$/ml was calculated with the Reed–Muench method (Reed and Muench, 1938).

SARS-CoV-2 Infection

One day prior to infection, Vero cells (10,000 cells), VeroE6/TMPRSS2 cells (10,000 cells), HeLa-ACE2/TMPRSS2 cells (10,000 cells) were seeded into a 96-well plate. SARS-CoV-2 (100 $TCID_{50}$) was inoculated and incubated at 37°C for 1 h. The infected cells were washed, and 180 µl of culture medium was added. The culture supernatant (10 µl) was harvested at indicated time points and used for real-time RT-PCR to quantify the viral RNA copy number. To monitor the syncytia formed in infected cell culture, the bright-field photos were obtained using ECLIPSE Ts2 (Nikon). The size of floating syncytia was measured by "quick selection tool" in Photoshop CS5 (Adobe) as pixel, and the area of floating syncytia was calculated from the pixel value.

Immunofluorescence Staining

One day prior to infection, VeroE6/TMPRSS2 cells (200,000 cells) were seeded on the coverslips put in 12-well plate and were infected with SARS-CoV-2 at MOI 0.01. At 48 hours postinfection, the cells were fixed with 4% paraformaldehyde in phosphate buffer saline (PBS) (Nacalai Tesque, Cat# 09154-85) for 10 min at room temperature. The fixed cells were permeabilized with 0.1% Triton X-100 in PBS for 10 min, blocked with 10% FBS in PBS for overnight at 4°C, and then stained using mouse anti-SARS-CoV-2 N monoclonal antibody (GeneTex, Cat# GTX632269) for 1 h. After washing three times with PBS, cells were incubated with an Alexa 488-conjugated anti-mouse IgG antibody (Jackson ImmunoResearch, Cat# 015-540-003) for 1 h. Nuclei were stained with Hoechst 33342 (Thermo Fisher Scientific, Cat# H3570). The coverslips were mounted on glass slides using Fluoromount-G (Southern Biotechnology, Cat# 0100-01) with Hoechst 33342. Fluorescence microscopy was performed on a confocal laser microscope (A1RSi, Nikon) and captured with NIS-Elements AR software (Nikon). The area of N-positive cells was quantified using Fiji software implemented in Image J.

SARS-CoV-2 Reverse Genetics

Recombinant SARS-CoV-2 was generated by circular polymerase extension reaction (CPER) as previously described (Motozono et al., 2021; Torii et al., 2021). In brief, 9 DNA fragments encoding the partial genome of SARS-CoV-2 (strain WK-

521, PANGO lineage A; GISAID ID: EPI_ISL_408667) (Matsuyama et al., 2020) were prepared by PCR using PrimeSTAR GXL DNA polymerase (Takara, cat# R050A). A linker fragment encoding hepatitis delta virus ribozyme, bovine growth hormone polyA signal and cytomegalovirus promoter was also prepared by PCR. The corresponding SARS-CoV-2 genomic region and the templates and primers of this PCR are summarized in **Table S3**. The 10 obtained DNA fragments were mixed and used for CPER (Torii et al., 2021).

To produce recombinant SARS-CoV-2, the CPER products were transfected into HEK293-C34 cells using TransIT-LT1 (Takara, cat# MIR2300) according to the manufacturer's protocol. At one day posttransfection, the culture medium was replaced with Dulbecco's modified Eagle's medium (high glucose) (Sigma-Aldrich, cat# R8758-500ML) containing 2% FCS, 1% PS and doxycycline (1 μg/ml; Takara, cat# 1311N). At six days posttransfection, the culture medium was harvested and centrifuged, and the supernatants were collected as the seed virus. To remove the CPER products (i.e., SARS-CoV-2-related DNA), 1 ml of the seed virus was treated with 2 μl TURBO DNase (Thermo Fisher Scientific, cat# AM2238) and incubated at 37°C for 1 h. Complete removal of the CPER products (i.e., SARS-CoV-2-related DNA) from the seed virus was verified by PCR. The working virus was prepared by using the seed virus as described above.

To generate recombinant SARS-CoV-2 mutants, mutations were inserted in fragment 8 (**Table S3**) using the GENEART site-directed mutagenesis system (Thermo Fisher Scientific, cat# A13312) according to the manufacturer's protocol with the following primers: Fragment 8_S D614G forward, 5'-CCA GGT TGC TGT TCT TTA TCA GGG TGT TAA CTG CAC AGA AGT CCC TG-3'; Fragment 8_S D614G reverse, 5'- CAG GGA CTT CTG TGC AGT TAA CAC CCT GAT AAA GAA CAG CAA CCT GG -3'; Fragment 8_S P681R forward, 5'-AGA CTC AGA CTA ATT CTC GTC GGC GGG CAC GTA GTG TA-3'; and Fragment 8_S P681R reverse, 5'-TAC ACT ACG TGC CCG CCG ACG AGA ATT AGT CTG AGT CT-3', according to the manufacturer's protocol. Nucleotide sequences were determined by a DNA sequencing service (Fasmac), and the sequence data were analyzed by Sequencher version 5.1 software (Gene Codes Corporation). The CPER for the preparation of SARS-CoV-2 mutants was performed using mutated fragment 8 instead of parental fragment 8. Subsequent experimental procedures correspond to the procedure for parental SARS-CoV-2 preparation (described above). To verify insertion of the mutation in the working viruses, viral RNA was extracted using a QIAamp viral RNA mini kit (Qiagen, cat# 52906) and reverse transcribed using SuperScript III reverse transcriptase (Thermo Fisher Scientific, cat# 18080085) according to the manufacturers' protocols. DNA fragments including the mutations

inserted were obtained by RT-PCR using PrimeSTAR GXL DNA polymerase (Takara, cat# R050A) and the following primers: WK-521 23339-23364 forward, 5'-GGT GGT GTC AGT GTT ATA ACA CCA GG-3'; and WK-521 24089-24114 reverse, 5'-CAA ATG AGG TCT CTA GCA GCA ATA TC-3'. Nucleotide sequences were determined as described above, and sequence chromatograms (**Figure 2A**) were visualized using the web application Tracy (https://www.gear-genomics.com/teal/) (Rausch et al., 2020).

Real-Time RT-PCR

Real-time RT-PCR was performed as previously described (Motozono et al., 2021; Shema Mugisha et al., 2020). Briefly, 5 µl of culture supernatant was mixed with 5 µl of 2 × RNA lysis buffer [2% Triton X-100, 50 mM KCl, 100 mM Tris-HCl (pH 7.4), 40% glycerol, 0.8 U/µl recombinant RNase inhibitor (Takara, cat# 2313B)] and incubated at room temperature for 10 min. RNase-free water (90 µl) was added, and the diluted sample (2.5 µl) was used as the template for real-time RT-PCR performed according to the manufacturer's protocol using the One Step TB Green PrimeScript PLUS RT-PCR kit (Takara, cat# RR096A) and the following primers: Forward *N*, 5'-AGC CTC TTC TCG TTC CTC ATC AC-3'; and Reverse *N*, 5'-CCG CCA TTG CCA GCC ATT C-3'. The copy number of viral RNA was standardized with a SARS-CoV-2 direct detection RT-qPCR kit (Takara, cat# RC300A). The fluorescent signal was acquired using a QuantStudio 3 Real-Time PCR system (Thermo Fisher Scientific), a CFX Connect Real-Time PCR Detection system (Bio-Rad) or a 7500 Real Time PCR System (Applied Biosystems).

Plasmid Construction

A plasmid expressing the SARS-CoV-2 S D614G protein was prepared in our previous study (Ozono et al., 2021). A plasmid expressing the SARS-CoV-2 D614G/P681R S protein (pC-S-D614G/P681R) was generated by site-directed mutagenesis PCR using pC-SARS2-S D614G (Ozono et al., 2021) as the template and the following primers listed in **Table S4**. The resulting PCR fragment was digested with KpnI and NotI and inserted into the KpnI-NotI site of the pCAGGS vector (Niwa et al., 1991).

Pseudovirus Assay

Pseudovirus assay was performed as previously described (Motozono et al., 2021; Ozono et al., 2021). Briefly, the pseudoviruses, lentivirus (HIV-1)-based, luciferase-expressing reporter viruses pseudotyped with the SARS-CoV-2 S protein and its derivatives, HEK293T cells (1×10^6 cells) were cotransfected with 1 µg of psPAX2-

IN/HiBiT (Ozono et al., 2020), 1 μg of pWPI-Luc2 (Ozono et al., 2020), and 500 ng of plasmids expressing parental S or its derivatives using Lipofectamine 3000 (Thermo Fisher Scientific, Cat# L3000015) or PEI Max (Polysciences, Cat# 24765-1) according to the manufacturer's protocol. At two days posttransfection, the culture supernatants were harvested, centrifuged. The amount of pseudoviruses prepared was quantified using the HiBiT assay as previously described (Ozono et al., 2021; Ozono et al., 2020). The pseudoviruses prepared were stored at –80°C until use. For the experiment, HOS-ACE2 cells and HOS-ACE2/TMPRSS2 cells (10,000 cells/50 μl) were seeded in 96-well plates and infected with 100 μl of the pseudoviruses prepared at 4 different doses. At two days postinfection, the infected cells were lysed with a One-Glo luciferase assay system (Promega, Cat# E6130), and the luminescent signal was measured using a CentroXS3 plate reader (Berthhold Technologies) or GloMax explorer multimode microplate reader 3500 (Promega).

Western blotting

Western blotting was performed as previously described (Ikeda et al., 2019; Ikeda et al., 2018; Sultana et al., 2019). To quantify the level of the cleaved S2 protein in the cells, the harvested cells were washed and lysed in lysis buffer [25 mM HEPES (pH 7.2), 20% glycerol, 125 mM NaCl, 1% Nonidet P40 substitute (Nalacai Tesque, Cat# 18558-54), protease inhibitor cocktail (Nalacai Tesque, Cat# 03969-21)]. After quantification of total protein by protein assay dye (Bio-Rad, Cat# 5000006), lysates were diluted with 2 × sample buffer [100 mM Tris-HCl (pH 6.8), 4% SDS, 12% β-mercaptoethanol, 20% glycerol, 0.05% bromophenol blue] and boiled for 10 min. Ten microliter of the samples (50 μg of total protein) were subjected to western blotting. To quantify the level of the cleaved S2 protein on virions, 900 μl of the culture medium including the pseudoviruses were layered onto 500 μl of 20% sucrose in PBS and centrifuged at 20,000 × g for 2 h at 4°C. Pelleted virions were resuspended in 1× NuPAGE LDS sample buffer (Thermo Fisher Scientific, Cat# NP0007) containing 2% β-mercaptoethanol, and the lysed virions were subjected to western blotting. For the protein detection, following antibodies were used: mouse anti-SARS-CoV-2 S monoclonal antibody (clone 1A9, GeneTex, Cat# GTX632604), rabbit anti-ACTB monoclonal antibody (clone 13E5, Cell Signaling, Cat# 4970), mouse anti-HIV-1 p24 monoclonal antibody (clone 183-H12-5C, obtained from the HIV Reagent Program, NIH, Cat# ARP-3537), horseradish peroxidase (HRP)-conjugated donkey anti-rabbit IgG polyclonal antibody (Jackson ImmunoResearch, Cat# 711-035-152), and HRP-conjugated donkey anti-mouse IgG polyclonal antibody (Jackson ImmunoResearch, Cat# 715-035-150). Chemiluminescence was

detected using SuperSignal West Femto Maximum Sensitivity Substrate (Thermo Fisher Scientific, Cat# 34095) or Western BLoT Ultra Sensitive HRP Substrate (Takara, Cat# T7104A) according to the manufacturers' instruction. Bands were visualized using the image analyzer, Amersham Imager 600 (GE Healthcare), and the band intensity was quantified using Image Studio Lite (LI-COR Biosciences) or Image J.

SARS-CoV-2 S-Based Fusion Assay

The SARS-CoV-2 S-based fusion assay was performed as previously described (Motozono et al., 2021). This assay utilizes a dual split protein (DSP) encoding *Renilla* luciferase (RL) and *GFP* genes, and the respective split proteins, DSP_{1-7} and DSP_{8-11}, are expressed in effector and target cells by transfection (Ikeda et al., 2018; Kondo et al., 2011). Briefly, on day 1, effector cells (i.e., S-expressing cells) and target cells (i.e., ACE2-expressing cells) were prepared at a density of 0.6 to 0.8 × 10^6 cells in a 6 well plate. To prepare effector cells, HEK293 cells were cotransfected with the expression plasmids for D614G S or D614G/P681R (400 ng) with $pDSP_{1-7}$ (400 ng) using TransIT-LT1 (Takara, Cat# MIR2300). To prepare target cells, HEK293 cells were cotransfected with pC-ACE2 (200 ng) and $pDSP_{8-11}$ (400 ng). In addition to the plasmids above, selected wells of target cells were also cotransfected with pC-TMPRSS2 (40 ng). On day 3 (24 h posttransfection), 16,000 effector cells were detached and reseeded into 96-well black plates (PerkinElmer, Cat# 6005225), and target cells were reseeded at a density of 1,000,000 cells/2 ml/well in 6-well plates. On day 4 (48 h posttransfection), target cells were incubated with EnduRen live cell substrate (Promega, Cat# E6481) for 3 h and then detached, and 32,000 target cells were applied to a 96-well plate with effector cells. RL activity was measured at the indicated time points using a Centro XS3 LB960 (Berthhold Technologies). The S proteins expressed on the surface of effector cells were stained with rabbit anti-SARS-CoV-2 S monoclonal antibody (GeneTex, Cat# GTX635654) and APC-conjugated goat anti-rabbit IgG polyclonal antibody (Jackson ImmunoResearch, Cat# 111-136-144). Normal rabbit IgG (SouthernBiotech, Cat# 0111-01) was used as a negative control. Expression levels of surface S proteins were analyzed using a FACS Canto II (BD Biosciences). RL activity was normalized to the mean fluorescence intensity (MFI) of surface S proteins, and the normalized values are shown as fusion activity.

Mathematical Modeling for Fusion Velocity Quantification

The following cubic polynomial regression model was employed to fit each of time-series datasets (**Figure 4E**):

$$y \sim b_0 + b_1 x + b_2 x^2 + b_3 x^3$$

The initial velocity of cell fusion was estimated from the derivative of the fitted cubic curve.

Neutralization Assay

Virus neutralization assay was performed on HOS-ACE2/TMPRSS2 cells using the SARS-CoV-2 S pseudoviruses expressing luciferase (see "Pseudovirus Assay" above). The viral particles pseudotyped with D614G S or D614G/P681R S were incubated with serial dilution of heat-inactivated human serum samples or the RBD-targeting NAbs (clones 8A5, 4A3 and CB6; Elabscience) at 37°C for 1 h. The pseudoviruses without sera and NAbs were also included. Then, the 80 μl mixture of pseudovirus and sera/NAbs was added into HOS-ACE2/TMPRSS2 cells (10,000 cells/50 μl) in a 96-well white plate and the luminescence was measured as described above (see "Pseudovirus Assay" above). 50% neutralization titer (NT_{50}) was calculated using Prism 9 (GraphPad Software).

For the cell-cell fusion neutralization assay, effector cells of the S-based fusion assay (i.e., S-expressing cells) were incubated with the serially diluted neutralizing antibodies targeting RBD (clones 8A5, 4A3 and CB6; Elabscience) at 37°C for 1 h. Then, target cells were applied and performed the S-based fusion assay as described above (see "SARS-CoV-2 S-Based Fusion Assay" above).

QUANTIFICATION AND STATISTICAL ANALYSIS

Data analyses were performed using Prism 9 (GraphPad Software). Data are presented as average with SD. In the figures except **Figure 5B**, n represents the number of technical replicate. In Figure 5B, n represents the number of serum donor.
In **Figure 2A, 3B, 4B, 4D, 4E**, statistically significant differences were determined by Student's t test.
In **Figures 2B and 2C**, statistically significant differences were determined by the Mann-Whitney U test.
In **Figures 4F and 4G**, statistically significant differences were determined by were determined by two-sided Welch's *t* test.
In **Figure 5B**, a statistically significant difference was determined by Wilcoxon matched-pairs signed rank test.